

Visualization and structural analysis of the bacterial magnetic organelle magnetosome using atomic force microscopy

メタデータ	言語: eng 出版者: 公開日: 2017-10-03 キーワード (Ja): キーワード (En): 作成者: メールアドレス: 所属:
URL	https://doi.org/10.24517/00010925

1 To be resubmitted for The Proceedings of the National Academy of Sciences USA.

2

3 *Classification:* BIOLOGICAL SCIENCE; Microbiology

4 Revision for MS# 2010-01870

5

6 **Visualization and structural analysis of the bacterial magnetic**
7 **organelle ‘magnetosome’ using atomic force microscopy**

8

9 Daisuke Yamamoto^{**†¶}, Azuma Taoka^{‡¶}, Takayuki Uchihashi^{*†}, Hideaki Sasaki[‡], Hiroki
10 Watanabe^{*}, Toshio Ando^{*†§||}, and Yoshihiro Fukumori^{‡||**}

11

12 ^{*} Department of Physics, Kanazawa University, Kakuma-machi, Kanazawa 920-1192,
13 Japan. [†]CREST, JST, Sanban-cho, Chiyoda-ku, Tokyo 102-0075, Japan. [‡]Department of
14 Life Science, Graduate School of Natural Science and Technology, Kanazawa
15 University, Kakuma-machi, Kanazawa 920-1192, Japan. [§]Frontier Science Organization,
16 Kanazawa University, Kakuma-machi, Kanazawa 920-1192, Japan.

17

18 *Corresponding author:*

19 ^{**}Yoshihiro Fukumori, Department of Life Science, Graduate School of Natural Science
20 and Technology, Kanazawa University, Kakuma-machi, Kanazawa 920-1192, Japan.

21 tel.: +81 76 264 6231; fax: +81 76 264 6230; e-mail:
22 fukumor@kenroku.kanazawa-u.ac.jp

23

24 *Manuscript information:* 30 pages, 6 figures, 0 table

25

26 *Footnotes:* ¶D.Y. and A.T. contributed equally to this work. ||T.A. and Y.F. contributed
27 equally to this work.

28

29 *Keywords:* atomic force microscopy, bacterial organelle, magnetosome, magnetotactic
30 bacteria, TPR protein

31 **Abstract**

32

33 The unique ability of magnetotactic bacteria to navigate along a geomagnetic field is
34 accomplished with the help of prokaryotic organelles, magnetosomes. The
35 magnetosomes have well-ordered chain-like structures, comprising
36 membrane-enveloped, nano-sized magnetic crystals, and various types of specifically
37 associated proteins. In this study, we applied atomic force microscopy (AFM), for the
38 first time, to investigate the spatial configuration of isolated magnetosomes from
39 *Magnetospirillum magneticum* AMB-1 in near-native buffer conditions. AFM
40 observation revealed organic material with a ~7 nm thickness surrounding a magnetite
41 crystal. Small globular proteins, identified as magnetosome-associated protein MamA,
42 were distributed on the mica surface around the magnetosome. Immuno-labeling with
43 AFM showed that MamA is located on the magnetosome surface. *In vitro* experiments
44 showed that MamA proteins interact with each other and form a high molecular mass
45 complex. These findings suggest that magnetosomes are covered with MamA oligomers
46 in near-native environments. Furthermore, nanodissection revealed that magnetosomes
47 are built with heterogeneous structures that comprise the organic layer. This study
48 provides important clues to the supramolecular architecture of the bacterial organelle,
49 the magnetosome, and insight into the function of the proteins localized in the organelle.

50 ¶body

51 **Introduction**

52

53 Magnetosomes are unique prokaryotic organelles synthesized in magnetotactic
54 bacteria, which function as a cellular compass to navigate along the Earth's magnetic
55 field (1-4). Proteomic analyses of the isolated magnetosomes indicate that the
56 magnetosome contains various types of specific associated proteins (5-7). Most of the
57 magnetosome-associated proteins are encoded in gene clusters within a genetic
58 'magnetosome island', which is essential for the synthesis of magnetosomes (8-11).
59 These proteins are thought to function in magnetite biomineralization, magnetic sensing,
60 formation of the magnetosome vesicle, and in the construction of magnetosomal
61 structures.

62 Insights into the magnetosome structure were provided using transmission electron
63 microscopic (TEM) techniques such as negative staining, freeze-etching, and
64 cryo-electron microscopy (12-17). These studies demonstrated that magnetosomes are
65 highly ordered structures. Magnetosomes comprise a chain of regular-sized
66 bio-mineralized magnetite crystals, each of which is surrounded by a lipid bilayer
67 membrane and organic components. Also, individual magnetosome particles are
68 connected by interparticle structures. Furthermore, most magnetosomes are arranged
69 intimately along novel cytoskeletal filaments as visualized by cryo-electron tomography
70 (14, 15, 18-20).

71 While a number of important findings about the magnetosome structure have been
72 provided by TEM, there are some disadvantages associated with TEM techniques. TEM
73 techniques require sample preparation methods such as fixation, staining, dehydration,
74 embedding, and thin sectioning, all of which may potentially damage or alter the native

75 structure of biologic specimens. Cryo-electron microscopy does not have these
76 disadvantages, and allows visualization of cellular structures in a near-native, frozen
77 hydrated states. Using this method, 3-4 nm resolution has been achieved for putative
78 cytoskeletal filaments in magnetotactic bacteria (14). However, in most of the precedent
79 studies, extraction of fine geometries is prevented for low electron density materials in a
80 crowded environment, such as membrane-embedded proteins surrounded by lipid
81 molecules. This is probably because of the low electron dose that must be used with
82 frozen hydrated materials, which results in a low signal-to-noise ratio of the projection
83 images (21). As a complementary technique, atomic force microscopy (AFM) has been
84 used to visualize organic samples ranging from single molecules to living cells under
85 physiologic conditions (22-24). In the AFM, the surface profile of the sample is imaged
86 by detecting the interaction between the sample and the AFM stylus during the raster
87 scanning of the sample. With this imaging technique, biologic molecules can be
88 visualized with a high signal-to-noise ratio. Remarkably, AFM allows for molecular
89 resolution imaging of organelles such as bacterial photosynthetic membranes (25) and
90 disk membranes (26). These AFM studies elucidated the organization of networks of
91 constituent molecules in the native membranes, which has been difficult using other
92 methods.

93 Of particular importance is the identification of the proteinaceous supramolecular
94 structure of the magnetosome. Due to its ability to visualize biologic specimens in their
95 near-native conditions with a high signal-to-noise ratio, AFM can be feasibly used to
96 visualize the constitutions of submicron-sized bacterial organelles at molecular
97 resolution. Here, we applied AFM to investigate the spatial configuration of
98 magnetosomes from *Magnetospirillum magneticum* AMB-1. AFM observations

99 indicated that the thickness of the organic layer wrapped around the magnetite crystal
100 was ~7 nm, and magnetosome-associated protein MamA was localized at the surface of
101 the organic layer. *In vitro* experiments revealed that MamA proteins interact with each
102 other to form a high molecular mass complex. Moreover, reconstruction experiment of
103 MamA showed a possibility that MamA may contribute to stabilize the magnetosome
104 chain structure as observed using AFM.

105 **Results**

106

107 **Structure of the purified magnetosome.** In the present study, hydrophilic bare mica
108 and hydrophobilized mica were served as substrates for AFM observations. These
109 surfaces have different affinities for the magnetosomes and magnetosome-associated
110 proteins, as described below. Thus, we used both substrates depending on the object of
111 interest. Although magnetosomes were observed on both substrates, magnetosomes
112 were more efficiently attached to the hydrophobilized mica surface than the bare mica
113 surface.

114 Figure 1A shows an AFM image of the purified magnetosomes adsorbed on the
115 hydrophobilized mica. The chain-like structure of magnetosomes observed by AFM was
116 consistent with that observed by TEM (16). To estimate the organic layer surrounding
117 the magnetite crystals, the height of the magnetosomes and the size of the magnetite
118 crystals were measured vertically along the magnetosome chains using AFM and TEM,
119 respectively. The height of each magnetosome particle was 60.8 ± 7.1 nm (n=404),
120 whereas the crystal size of the magnetite was 46.9 ± 6.9 nm (n=298) in diameter. This
121 finding indicated that the individual magnetite crystal is surrounded with ~ 7 nm of an
122 electron permeable layer composed of organic components.

123 Regular-sized globular particles were found to be dispersed on the bare mica (Fig.
124 1B), while these particles were not observed around magnetosomes on the
125 hydrophobilized mica. Removal of the particles could not be achieved by further
126 purification of the magnetosomes. Moreover, the particles were not observed around the
127 magnetosomes when the magnetosomes were chemically cross-linked with
128 glutaraldehyde before deposition onto the bare mica. These results strongly suggest that

129 the particles originated from the magnetosomes. Another architectural feature observed
130 by AFM was a sheet-like structure in the proximity of the magnetosomes (asterisk in
131 Fig. 1B). This sheet-like structure was observed on both bare mica and hydrophobilized
132 mica. The thickness of the sheet-like structures was approximately 3 nm.

133 The surface of the magnetosome was closely examined by simultaneously obtaining
134 topographic and phase images (Fig. 1CD). In the topographic image, detailed surface
135 structures were difficult to visualize. In contrast, a clear contrast was obtained in the
136 phase image. The phase image showed texture with granular and wrinkled lines on the
137 magnetosome vesicle. The phase contrast of AFM is strongly relevant to several surface
138 properties such as viscoelasticity, elasticity and surface adhesion energy (27). The phase
139 imaging mode allows one to visualize compositional variation, even for the sample that
140 the fine structures are difficult to visualize in the topographic images. Therefore, the
141 phase contrast shown in Fig. 1D should represent heterogeneity in the sample, and
142 suggests that the outermost layer of magnetosomes is formed by an amorphous layer of
143 magnetosome-associated proteins.

144

145 **Identification of globular particles observed on bare mica.** To understand the
146 origination of the small particles (Fig. 1B and 2A), we treated magnetosomes with
147 alkaline buffer. As reported previously, magnetosomal protein MamA (Mam22) and
148 cytochrome *cd*₁ are efficiently solubilized from magnetosomes by alkaline buffer (13).
149 When the alkaline-treated magnetosomes were loaded onto the bare mica, the small
150 particles were not observed (Fig. 2B), whereas a number of particles were observed on
151 the bare mica when the spent alkaline solution was used as a sample (Fig. 2C). In
152 contrast, the sheet-like structures were not removed by the alkaline-treatment (Fig. S1).

153 Before the alkaline treatment, the height distribution of the particles showed two clear
154 peaks on the histogram (Fig. 2E). Most of the particles were ~3 nm in height, and 6 to
155 8-nm particles were also detected. The mean height of the particles solubilized from
156 magnetosomes (Fig. 2F) was in good agreement with the major distribution of the
157 particles observed before the alkaline treatment.

158 To identify the small particles, proteins attached to the bare mica were analyzed. A
159 24-kDa protein band was detected by sodium dodecyl sulfate (SDS)-polyacrylamide gel
160 electrophoresis (SDS-PAGE) analysis of samples extracted from the mica (Fig. 2H), and
161 was positively recognized by anti-MamA antibody (Fig. 2I). To further examine the
162 correlation of MamA protein with the globular particles, we observed the purified
163 magnetosomes from the $\Delta mamA$ mutant of *M. magneticum* AMB-1 (28). In this case,
164 the number density of the particles observed on the bare mica significantly reduced (Fig.
165 2DG). This clearly indicates that majority of the particles observed around
166 magnetosomes on bare mica are MamA molecules.

167 In addition to structural imaging, the AFM stylus can be used as a manipulator to
168 dissect individual biologic samples (29, 30). Figure 3 and the supplemental movie show
169 high-speed AFM images of the dissection process of the magnetosomes observed on the
170 bare mica. While the magnetosomes were being imaged, additional tapping force was
171 applied (20 – 33 frames). The magnetosomes were removed by the scanning stylus.
172 Consequently, sheet-like structures appeared at the initial position of the magnetosome
173 (Fig. 3, asterisks). The appearance and thickness (3 nm) of these sheets were consistent
174 with those of the sheets observed in the proximity of magnetosomes (Fig. 1B). These
175 sheets seem to be lipid bilayers, based on their featureless surface structure and
176 thickness that is comparable to the typical value of lipid membranes (3-4 nm) measured

177 by X-ray scattering (31) and AFM (26). Together with the sheet-like structures,
178 additional small particles, which were 3 nm in height, were observed around the
179 magnetosomes after the dissection (Fig. 3, arrowheads). These findings indicated that
180 magnetosomes contain heterogeneous structures that should comprise the organic layer.

181

182 **Oligomerization of MamA.** MamA, one of the most abundant proteins in the
183 magnetosome, contains five or six tetratricopeptide repeat (TPR) motifs (32, 33) that
184 mediate the protein-protein interactions to assemble the multiprotein complexes (34).
185 Therefore, MamA may function as a receptor for the protein-protein interaction in
186 magnetosomes. We examined the partner protein of MamA using *M. magnetotacticum*
187 MS-1. *M. magnetotacticum* MS-1 is very closely related with *M. magneticum* AMB-1.
188 The amino acid sequences of *M. magnetotacticum* MamA (MamA_{MS-1}: known as
189 Mam22: BAA11643) and *M. magneticum* AMB-1 MamA (MamA_{AMB-1}: known as
190 Mms24: BAE49775) are identical.

191 For the isolation of MamA-associated proteins, the recombinant N-terminal
192 his-tagged MamA_{MS-1} (His-MamA) was chemically conjugated with the resin to prepare
193 MamA-affinity column. We subjected solubilized magnetosome-associated proteins
194 from *M. magnetotacticum* MS-1 to the MamA-affinity column. MamA affinity column
195 chromatography showed that one major-protein band (23.6 kDa) and four-minor protein
196 bands (26.8 kDa, 31.6 kDa, 54.0 kDa and 63.5 kDa) were eluted (Fig. 4A). The
197 23.6-kDa protein was identified to be MamA_{MS-1} by immunoblotting (Fig. S2).
198 Unfortunately, the N-terminal amino acid sequences of the four minor-protein bands
199 were not determined because the amounts of these proteins were not sufficient to
200 analyze. To confirm this result, a pull-down assay was performed. MamA_{MS-1} was

201 co-precipitated with His-MamA (Fig. 4B). These results indicated that MamA proteins
202 interact with each other and form an oligomeric complex.

203 We examined the oligomerization status of the recombinant MamA. Purified
204 His-MamA was separated by gel filtration into a single peak, which was estimated to be
205 560 kDa (Fig. S3). To further analyze the oligomeric status of His-MamA, we examined
206 the peak fractions of the gel filtration by AFM. On the bare mica, we observed small
207 particles (~3 nm in height), similar to that shown in Fig. 2A, instead of a large complex
208 (Fig. S4). In contrast, His-MamA oligomers were visualized on
209 aminosilane-functionalized mica (AP-mica). The AFM image of oligomerized
210 His-MamA revealed a unique configuration: a regular-sized rugged-shaped globular
211 structure (Fig. 4CD). The size of the observed complex ranged from 4.5 to 6.5 nm in
212 height and 14 to 20 nm in diameter. This agrees with the molecular mass estimated from
213 the gel filtration column chromatography.

214

215 **Localization of MamA protein complexes in the magnetosomes.** Immuno-labeling
216 was performed to identify the location of MamA_{AMB-1} in the magnetosomes using AFM.
217 Figure 5A shows an AFM image of the magnetosomes labeled with anti-MamA
218 antibodies. After labeling, antibodies bound densely to magnetosomes. By contrast,
219 pre-immune serum, which has no significant affinity for MamA, had no effect on the
220 appearance of the magnetosomes (Fig. 5B). The dense packing of the antibodies on the
221 magnetosomes indicated that a considerable amount of MamA_{AMB-1} was located at the
222 outermost layer of the magnetosomes. The dimension of magnetosomes significantly
223 increased from 57.2 ± 7.8 nm (n=25) to 72.7 ± 10.8 nm (n=69) in height, and from 59.2
224 ± 7.6 nm (n=25) to 90.7 ± 15.8 nm (n=69) in width after labeling with anti-MamA

225 antibody (Fig. 5CD). The height difference between labeled and non-labeled
226 magnetosomes (15 nm) was in good agreement with the diameter of the antibody (35).

227 A previous study has indicated that the recombinant His-MamA can attach to the
228 MamA-eliminated magnetosomes prepared by the alkaline treatment (13). To elucidate
229 the location of reconstructed His-MamA in the magnetosomes, immuno-labeling was
230 performed for both alkaline-treated and MamA-reconstructed magnetosomes. The
231 anti-MamA antibody failed to bind to the alkaline-treated magnetosomes (Fig. 5E). This
232 shows the depletion of MamA_{AMB-1} from the magnetosomes by the treatment. After the
233 reconstruction of the His-MamA to the alkaline-treated magnetosomes, antibodies
234 densely bound to magnetosomes (Fig. 5F). The appearance of the immuno-labeled
235 His-MamA-reconstructed magnetosomes was very similar to that of the untreated
236 magnetosomes. This result suggests that the endogenous MamA_{AMB-1} and the
237 recombinant His-MamA share the binding site on the magnetosomes.

238

239 **Effect of MamA elimination on the chain structure.** To examine the effect of MamA
240 elimination on the chain structure of magnetosomes, spacing between magnetosome
241 particles was compared between the intact magnetosomes and MamA-eliminated
242 magnetosomes prepared by alkaline treatment (Fig. 6A). The averaged center-to-center
243 distance between the adjacent particles in the intact magnetosomes (59.4 ± 6.2 nm
244 [n=364]) was consistent with the spacing between magnetite crystals observed in cell
245 using cryo-TEM (28). Interestingly, the averaged distance between the particles of
246 alkaline-treated magnetosomes significantly increased ($P < 0.0001$: estimated using F
247 test) by 3~4 nm (62.8 ± 7.8 nm [n=336]). On the other hand, the alkaline treatment had
248 no significant effect on the distance between the magnetosomes purified from Δ mamA

249 mutant (Fig. 6B). When the His-MamA was rebound to the alkaline-treated
250 magnetosomes, the spacing between the magnetosome particles decreased (58.5 ± 5.8
251 nm [n=172]) to the value consistent with that of the untreated magnetosomes (Fig. 6A).
252 The interparticle spacings of the untreated magnetosomes and the MamA reconstructed
253 magnetosomes showed no significant difference (P=0.35: estimated using F test). These
254 results indicate that MamA have an effect on the distance between magnetosomes.

255 **Discussion**

256 The aim of the present study is characterization of the structures and compositional
257 organization of magnetosomes in an aqueous environment using AFM. The spatial
258 localization, supramolecular organization, and functions of the individual components
259 within the magnetosome must be determined to understand how this bacterial organelle
260 functions as a magnetic compass. To date, AFM visualization of prokaryotic
261 intra-membrane structures at a spatial resolution close to one nm has been achieved for
262 flat membranes such as purple membrane (36), chromatophore (25, 37) and outer
263 membrane (38). It remains challenging, however, to obtain high-resolution images for a
264 whole organelle that contains various molecular species and has a complex
265 three-dimensional structure. Here, we visualized the near-native hemispherical
266 configuration of the isolated magnetosomes (Fig. 1). In the phase image, we were able
267 to discern the surface structure at a lateral resolution of 4 to 8 nm, which should
268 represent the molecular organization at the surface of the magnetosomes. Although this
269 resolution is insufficient to determine the precise molecular organization, the lateral
270 resolution obtained in this study is the best achieved so far for magnetosomal membrane
271 in buffer condition.

272 The AFM showed that the magnetosome was ~61 nm in height. On the other hand,
273 the crystal size of the magnetite was ~47 nm in diameter. Therefore, the thickness of the
274 electron permeable organic layer was calculated to be 7 nm. Although magnetite crystal
275 is enveloped by a lipid membrane, the thickness of the organic layer is significantly
276 larger than single bilayer membrane. This means that the magnetic particle is
277 surrounded by other organic components that may be composed of
278 magnetosome-associated proteins. A previous TEM observation has identified the

279 organic layer, termed the magnetosomal matrix (13). Based on the TEM observation,
280 the magnetosomal matrix spread around the magnetosome vesicles several tens of
281 nanometers in width. Instead of this huge structure, our AFM study revealed a thin
282 organic layer. The possible reason for this difference is the variation in surface
283 properties of the substrates or the imaging conditions between AFM and TEM.

284 The previous TEM observation has revealed also a fibrous texture that connects the
285 flanking magnetosome particles (13). In the present AFM study, however, this structure
286 was not observed in the magnetosome chains because of the difficulty of AFM to
287 precisely trace deep features. To profile surface morphologies in narrow spaces, the
288 AFM stylus must have both a high aspect ratio and a small apex radius. Otherwise, the
289 apex of the AFM stylus cannot access the fine structures at the bottom of the trough.
290 Although our AFM styli were sufficiently sharp to visualize the structure of the
291 magnetosomes, an extremely high aspect ratio will be needed to define the interparticle
292 connection.

293 As shown in Figure 4CD, we were able to visualize His-MamA oligomers on the
294 AP-mica, whereas small particles of 3 nm in height instead of large complexes were
295 observed on the bare mica (Fig. S4). This may be due to differences in the interaction
296 between the proteins and substrates. In addition to the particles of 3 nm in height, the
297 particles of 6 to 8 nm in height were also observed on the bare mica (Fig. 2E). These 6
298 to 8 nm particles are attributed to partially deoligomerized MamA complex, because
299 they were not observed around the magnetosomes from *mamA* mutant (Fig. 2G).
300 Moreover, these particles were not observed when the magnetosome was chemically
301 fixed before depositing onto the bare mica. Therefore, the MamA proteins easily
302 detached from magnetosomes in buffer conditions, indicating that MamA was loosely

303 bound by the magnetosomes.

304 The most striking finding in this study was that the magnetosome vesicles were
305 surrounded by MamA protein. The subcellular localization of MamA has been
306 previously demonstrated. MamA-green fluorescent protein was observed to localize as a
307 patchy line within the cell (3, 28). Also, immunogold staining with TEM showed that
308 MamA associates with the magnetosomal matrix (13). In this paper, the AFM imaging
309 of the immuno-labeled magnetosomes (Fig. 5) clearly indicated that MamA was located
310 at the surface of the organelle. The close packing of the anti-MamA antibodies on the
311 magnetosomes indicated that MamA protein densely covers the entire outer surface of
312 the magnetosome chain. As described above, the thickness of the organic layer covering
313 the magnetite is 7 nm. This value approximately coincides with the sum of the thickness
314 of the bilayer lipid membrane and the height of the MamA oligomer. This finding
315 supports the view that the magnetosome membrane vesicle is coated with MamA
316 oligomers. Although we attempted to visualize MamA complexes on the surface of
317 magnetosomes using bare mica and AP-mica as the substrates, we could not identify
318 individual MamA oligomers on the magnetosome. This is likely due to the texture of the
319 magnetosome surface, which is amorphous and closely packed with various types of
320 protein.

321 The TPR protein MamA most probably functions as a receptor that interacts with a
322 partner protein in the magnetosome. Our results showed that MamA interacts with
323 MamA itself to form oligomer (Fig. 4), and binds to the surface of magnetosomes (Fig.
324 5). In addition, MamA further interacts with unidentified proteins that were extracted
325 from the magnetosomes (Fig. 4A). These results suggest that MamA oligomers are
326 anchored on the magnetosome membrane through magnetosome membrane-associated

327 proteins, and partially through lipids of the magnetosome membrane. Because MamA is
328 abundant relative to other magnetosome-associated proteins, MamA oligomers would
329 be sparsely bound by the anchor proteins in the organic layer.

330 A previous study on $\Delta mamA$ mutant showed that the cells produce regular number
331 of magnetosome vesicles. However, not all these vesicles are functional for the
332 production of magnetite. Based on these observations, Komeili et al. proposed that
333 MamA is part of the magnetosome assembly and maintenance processes such as protein
334 sorting or activation of the magnetosome vesicles in response to external signals (28). In
335 this study, we presented that MamA is located at the outermost layer of magnetosomes.
336 With this spatial configuration of MamA in the magnetosomes, it is possible that MamA
337 act as a scaffold that links between the magnetosome vesicles and cytoplasmic factors
338 that activate the magnetite formation. Although our study showed a possibility that
339 MamA contributes to the stabilization of magnetosome chain (Fig. 6), it is unclear how
340 this stabilizing effect associates with magnetosome formation processes *in vivo*. Further
341 studies on molecular assembly and function of MamA would expand our understanding
342 of magnetosome formation.

343 It is now clear that bacteria are highly organized, possessing cytoskeletons, internal
344 compartments, and carefully positioned macromolecular machines. To understand how
345 they are organized and express their function, it is essential to unveil the ultrastructures
346 under near-native conditions. Here, we visualized one of the most complex bacterial
347 organelles, the magnetosome, in near-native conditions. To this end, AFM-based
348 techniques such as immuno-labeling and nanodissection procedures are powerful
349 approaches, as evidenced in this study. Combined with the possibility to reveal surface
350 structures with high lateral resolution, AFM will exploit the new avenue for the

351 investigation of the ultrastructures of prokaryotic organelles.

352 **Materials and Methods**

353

354 **Microorganisms and cultures.** *M. magneticum* AMB-1 (ATCC 700264), *mamA*
355 deletion mutant of AMB-1 (28), and *M. magnetotacticum* MS-1 (ATCC 31632) were
356 cultured in a liquid media under an O₂ (1%) - N₂ (99%) atmosphere at 25°C in the dark
357 (39). *Escherichia coli* strain BL21(DE3) (Novagen, Madison, WI) containing
358 pET15b-mam22 (32) was used for overproduction of His-tagged MamA. *E. coli* was
359 cultivated as described (13).

360

361 **Purification of recombinant His-MamA.** His-MamA was purified as described (32).
362 Purified His-MamA was subjected to gel filtration column chromatography (Sephacryl
363 S-300, GE Healthcare, Wauwatosa, WI). The apparent molecular mass was calculated
364 using a Gel Filtration Calibration Kit (GE Healthcare) as a standard.

365

366 **Magnetosome preparation.** Magnetosomes were purified as described (13) and used
367 immediately or stored at 4°C without freezing. Alkaline treatment of the purified
368 magnetosomes with 0.1 M Caps-NaOH buffer (pH 11.0) was performed as described
369 (13). TEM observation of the purified magnetosomes was performed using a JEOL JEM
370 2000EX TEM operating at 120 kV in bright-field mode. For reconstruction with
371 His-MamA, the alkaline treated magnetosomes (3 mg [wet weight]) were incubated
372 with the His-MamA (20 μM) in 200 μl of 10mM Tris-HCl (pH 8.0) at 25°C for 16 h,
373 and then centrifuged at 8,000 × *g* for 5 min. The pellets obtained were washed with 1
374 ml of 10 mM Tris-HCl buffer (pH 8.0), and centrifuged at 8,000 × *g* for 5 min. The
375 supernatant containing the unbound His-tagged His-MamA was removed by aspiration

376 and re-suspended in 10 mM Tris-HCl buffer (pH 8.0). This washing step was repeated
377 three times.

378

379 **Atomic force microscopy.** Imaging was performed with a laboratory-built high-speed
380 AFM, an extensively improved version of the previously reported AFM (40, 41). The
381 high-speed AFM was equipped with small cantilevers ($k = 0.1-0.2$ N/m, $f = 800-1200$
382 kHz in water) and operated in tapping mode. A lock-in amplifier (SR844-RF, Stanford
383 Research Systems, Sunnyvale, CA) was used to detect the phase difference between the
384 cantilever oscillation and the excitation signal. The AFM styli were grown on each
385 cantilever by electron beam deposition. Freshly cleaved mica, AP-mica, and
386 hydrophobilized mica were used as substrates. AP-mica was prepared by depositing
387 0.05 % 3-aminopropyltriethoxysilane (Shin-Eths Chemical, Japan) on freshly cleaved
388 mica and left for 3 min. Hydrophobilization of mica was performed using a vapor
389 deposition method, in which hexamethyldisilazane (Shin-Etsu Chemical) and the
390 freshly cleaved mica were placed simultaneously in a sealed container and incubated at
391 60 °C for 30 min. The purified magnetosomes ($OD_{600nm} = 7$) were adsorbed on the
392 substrates in 10 mM Tris-HCl (pH 8.0). After 3 min, the sample was rinsed with 10 mM
393 Tris-HCl (pH 8.0). For chemical fixation, the sample was incubated with 1 %
394 glutaraldehyde for 3 min. For immuno-labeling of MamA in the purified magnetosomes,
395 the magnetosomes were adsorbed on the hydrophobilized mica and then incubated with
396 1 % bovine serum albumin (BSA) in phosphate buffered saline (PBS) for 5 min.
397 Subsequently, the sample was incubated with anti-MamA rabbit polyclonal antibodies
398 or pre-immuno serum as described (13). After rinsing with PBS two times for 1 min
399 each, the specimens were chemically fixed with 1 % glutaraldehyde for 3 min in PBS.

400

401 **Identification of mica binding protein.** The magnetosome suspension ($OD_{600nm} = 7$)
402 was loaded onto a bare mica (76 x 26 mm), which was fixed on slide glass with
403 double-stick tape, and then incubated for 3 min. After the mica was washed three times
404 with 10 mM Tris-HCl (pH 8.0), the mica was sonicated with an ultrasonic oscillator
405 (Branson model 450; 20 kHz 10 W) to remove bound magnetosomes from the mica.
406 AFM confirmed that only a few magnetosomes were present on the mica surface, and a
407 large amount of the globular particles and a small amount of sheet-like structures
408 remained on the mica. The resulting mica was incubated with 2% SDS containing 10
409 mM Tris-HCl (pH 8.0). Based on AFM observation, most of the particles were removed
410 from the mica surface by SDS treatment. The proteins extracted from the mica were
411 analyzed by SDS-PAGE.

412

413 **MamA-affinity chromatography.** To prepare His-MamA affinity resin, 1 ml of
414 CNBr-activated Sepharose 4B (GE Healthcare) was coupled with the purified
415 His-MamA (1.2 mg). The His-MamA resin column (0.5 × 4 cm) was equilibrated with
416 10 mM Tris-HCl (pH 8.0) containing 0.1% sucrose monocaprato (equilibration buffer).
417 To solubilize magnetosome-associated proteins, the magnetosomes purified from *M.*
418 *magnetotacticum* MS-1 (~0.6 g, wet weight) were incubated with 10 ml of 10 mM
419 Tris-HCl (pH 8.0) containing 2% sucrose monocaprato at 4°C for 16 h. Then, the
420 suspension was centrifuged at 10,000 × *g* for 15 min at 4°C. After the resultant
421 supernatant was dialyzed against the equilibration buffer, the protein solution (12 ml)
422 was subjected to the His-MamA-column with a flow rate of 1 ml/hour. After that, the
423 column was washed with the equilibration buffer containing 1 M NaCl. Then the

424 binding proteins were eluted with 0.1 M Caps-NaOH buffer (pH 11.0) containing 0.1%
425 sucrose monooxalate from the column.

426

427 **Pull-down assay.** The solution of the His-MamA (50 μ l, 1 mg/ml) was mixed with 25
428 μ l of the Ni-NTA resin (Qiagen, Germantown, MD), which had been equilibrated with
429 the pull-down buffer (20 mM Tris-HCl [pH 8.0], 0.2 M NaCl, 5 mM imidazole). The
430 Ni-NTA resin with His-MamA was incubated with 350 μ l of the solubilized
431 magnetosome-associated proteins from *M. magnetotacticum* MS-1 (0.14 mg/ml), in
432 pull-down buffer at 25°C for 1 h. After the resin was washed three times with 1 ml of
433 the washing buffer (20 mM Tris-HCl [pH 8.0], 0.2 M NaCl, 60 mM imidazole), the
434 binding protein was eluted from the resin with 30 μ l of elution buffer (20 mM Tris-HCl,
435 [pH 8.0] 0.2 M NaCl, 250 mM imidazole), and analyzed by SDS-PAGE.

436

437 **Physical and chemical measurements.** The protein contents were determined using the
438 bicinchoninic acid method (BCA Protein Assay Kit, Pierce Chemical) with BSA as a
439 standard. SDS-PAGE was performed according to the method of Laemmli (42).
440 Immunoblotting analysis was performed as described (13).

441

442 We thank A. Komeili for providing the *mamA* deletion mutant of *M. magneticum*
443 AMB-1.

444 **References**

445

- 446 1. Bazylinski D-A, Frankel R-B (2004) Magnetosome formation in prokaryotes.
447 *Nat Rev Microbiol* 2:217-230.
- 448 2. Schüler D (2008) Genetics and cell biology of magnetosome formation in
449 magnetotactic bacteria. *FEMS Microbiol Rev* 32:654-672.
- 450 3. Komeili A (2007) Molecular mechanisms of magnetosome formation. *Annu Rev*
451 *Biochem* 76:351-366.
- 452 4. Faivre D, Schüler D (2008) Magnetotactic bacteria and magnetosomes. *Chem*
453 *Rev* 108:4875-4898.
- 454 5. Matsunaga T, *et al.* (2005) Complete genome sequence of the facultative
455 anaerobic magnetotactic bacterium *Magnetospirillum* sp. strain AMB-1. *DNA*
456 *Res* 12:157-166.
- 457 6. Grünberg K, *et al.* (2004) Biochemical and proteomic analysis of the
458 magnetosome membrane in *Magnetospirillum gryphiswaldense*. *Appl Environ*
459 *Microbiol* 70:1040-1050.
- 460 7. Matsunaga T, Okamura Y (2003) Genes and proteins involved in bacterial
461 magnetic particle formation. *Trends Microbiol* 11:536-541.
- 462 8. Schübbe S, *et al.* (2003) Characterization of a spontaneous nonmagnetic mutant
463 of *Magnetospirillum gryphiswaldense* reveals a large deletion comprising a
464 putative magnetosome island. *J Bacteriol* 185:5779-5790.
- 465 9. Ullrich S, Kube M, Schübbe S, Reinhardt R, Schüler D (2005) A hypervariable
466 130-kilobase genomic region of *Magnetospirillum gryphiswaldense* comprises a
467 magnetosome island which undergoes frequent rearrangements during stationary

- 468 growth. *J Bacteriol* 187:7176-7184.
- 469 10. Bazylinski D-A, Schübbe S (2007) Controlled biomineralization by and
470 applications of magnetotactic bacteria. in *Advances in Applied Microbiology*,
471 eds Laskin AI, Sariaslani S, Gadd GM (Academic Press, London), pp 21-62.
- 472 11. Richter M, *et al.* (2007) Comparative genome analysis of four magnetotactic
473 bacteria reveals a complex set of group-specific genes implicated in
474 magnetosome biomineralization and function. *J Bacteriol* 189:4899-4910.
- 475 12. Martins J-L, Keim C-N, Farina M, Kachar B, Lins U (2007) Deep-etching
476 electron microscopy of cells of *Magnetospirillum magnetotacticum*: Evidence
477 for filamentous structures connecting the magnetosome chain to the cell surface.
478 *Curr Microbiol* 54:1-4.
- 479 13. Taoka A, *et al.* (2006) Spatial localizations of Mam22 and Mam12 in the
480 magnetosomes of *Magnetospirillum magnetotacticum*. *J Bacteriol*
481 188:3805-3812.
- 482 14. Scheffel A, *et al.* (2006) An acidic protein aligns magnetosomes along a
483 filamentous structure in magnetotactic bacteria. *Nature* 440:110-114.
- 484 15. Komeili A, Li Z, Newman D-K, Jensen G-J (2006) Magnetosomes are cell
485 membrane invaginations organized by the actin-like protein MamK. *Science*
486 311:242-245.
- 487 16. Gorby Y-A, Beveridge T-J, Blakemore RP (1988) Characterization of the
488 bacterial magnetosome membrane. *J Bacteriol* 170:834-841.
- 489 17. Lins U, Farina M, Kachar B (2003) Membrane vesicles in magnetotactic
490 bacteria. *Microbiol Res* 158:317-320.
- 491 18. Taoka A, Asada R, Wu L-F, Fukumori Y (2007) Polymerization of the actin-like

- 492 protein MamK, which is associated with magnetosomes. *J Bacteriol*
493 189:8737-8740.
- 494 19. Pradel N, Santini C-L, Bernadac A, Fukumori Y, Wu L-F (2006) Biogenesis of
495 actin-like bacterial cytoskeletal filaments destined for positioning prokaryotic
496 magnetic organelles. *Proc Natl Acad Sci USA* 103:17485-17489.
- 497 20. Frankel R-B, Bazylinski D-A (2006) How magnetotactic bacteria make
498 magnetosomes queue up. *Trends Microbiol* 14:329-331.
- 499 21. Koster A-J, *et al.* (1997) Perspectives of molecular and cellular electron
500 tomography. *J Struct Biol* 120:276-308.
- 501 22. Dufrêne Y-F (2008) Towards nanomicrobiology using atomic force microscopy.
502 *Nat Rev Microbiol* 6:674-680.
- 503 23. Dufrêne Y-F (2004) Using nanotechniques to explore microbial surfaces. *Nat*
504 *Rev Microbiol* 2:451-460.
- 505 24. Engel A, Müller D-J (2000) Observing single biomolecules at work with the
506 atomic force microscope. *Nat Struct Biol* 7:715-718.
- 507 25. Bahatyrova S, *et al.* (2004) The native architecture of a photosynthetic
508 membrane. *Nature* 430:1058-1062.
- 509 26. Fotiadis D, *et al.* (2003) Rhodopsin dimers in native disc membranes. *Nature*
510 421:127-128.
- 511 27. García R, Magerle R, Perez R (2007) Nanoscale compositional mapping with
512 gentle forces. *Nat Mater* 6:405-411.
- 513 28. Komeili A, Vali H, Beveridge T-J, Newman D-K (2004) Magnetosome vesicles
514 are present before magnetite formation, and MamA is required for their
515 activation. *Proc Natl Acad Sci USA* 101:3839-3844.

- 516 29. Hansma H-G, *et al.* (1992) Reproducible imaging and dissection of plasmid
517 DNA under liquid with the atomic force microscope. *Science* 256:1180-1184.
- 518 30. Hoh J-H, Sosinsky G-E, Revel J-P, Hansma P-K (1993) Structure of the
519 extracellular surface of the gap junction by atomic force microscopy. *Biophys J*
520 65:149-163.
- 521 31. Mitra K, Ubarretxena-Belandia I, Taguchi T, Warren G, Engelman D-M (2004)
522 Modulation of the bilayer thickness of exocytic pathway membranes by
523 membrane proteins rather than cholesterol. *Proc Natl Acad Sci USA*
524 101:4083-4088.
- 525 32. Okuda Y, Fukumori Y (2001) Expression and characterization of a
526 magnetosome-associated protein, TPR-containing MAM22, in *Escherichia coli*.
527 *FEBS Lett* 491:169-173.
- 528 33. Okuda Y, Denda K, Fukumori Y (1996) Cloning and sequencing of a gene
529 encoding a new member of the tetratricopeptide protein family from
530 magnetosomes of *Magnetospirillum magnetotacticum*. *Gene* 171:99-102.
- 531 34. D'Andrea L-D, Regan L (2003) TPR proteins: the versatile helix. *Trends*
532 *Biochem Sci* 28:655-662.
- 533 35. Kienberger F, Mueller H, Pastushenko V, Hinterdorfer P (2004) Following single
534 antibody binding to purple membranes in real time. *EMBO Rep* 5:579-583.
- 535 36. Müller D-J, Schabert F-A, Büldt G, Engel A. (1995) Imaging purple membranes
536 in aqueous solutions at sub-nanometer resolution by atomic force microscopy.
537 *Biophys J* 68:1681-1686.
- 538 37. Scheuring S, *et al.* (2003) Nanodissection and high-resolution imaging of the
539 *Rhodospseudomonas viridis* photosynthetic core complex in native membranes

- 540 by AFM. *Proc Natl Acad Sci USA* 100:1690-1693.
- 541 38. Jarosławski S, Duquesne K, Sturgis J-N, Scheuring S (2009) High-resolution
542 architecture of the outer membrane of the Gram-negative bacteria *Roseobacter*
543 *denitrificans*. *Mol Microbiol* 74:1211-1222.
- 544 39. Blakemore R-P, Maratea D, Wolfe R-S (1979) Isolation and pure culture of a
545 freshwater magnetic spirillum in chemically defined medium. *J Bacteriol*
546 140:720-729.
- 547 40. Ando T, *et al.* (2001) A high-speed atomic force microscope for studying
548 biological macromolecules. *Proc Natl Acad Sci USA* 98:12468-12472.
- 549 41. Ando T, Uchihashi T, Fukuma T (2008) High-speed atomic force microscopy for
550 nano-visualization of dynamic biomolecular processes. *Prog Surf Sci*
551 83:337-437.
- 552 42. Laemmli U-K (1970) Cleavage of structural proteins during the assembly of the
553 head of bacteriophage T4. *Nature* 227:680-685.

554 **Figure legends**

555

556 Fig. 1. AFM observations of magnetosomes adsorbed on the mica surfaces. (A) An
557 AFM image of the magnetosomes chain adsorbed on a hydrophobilized mica surface.
558 (B) An AFM image of magnetosomes adsorbed on a bare mica surface. Small particles
559 (arrows) and a sheet-like structure (asterisk) were observed in the proximity of the
560 magnetosomes. High magnification (C) topographic and (D) phase contrast images of
561 the magnetosome particles on hydrophobilized mica. The AFM images were recorded at
562 imaging rates of (A) 2.1, (B) 1.0 and (C and D) 4.0 s/frame, and the number of pixels of
563 (A and B) 256×256 and (C and D) 150×150.

564

565 Fig. 2. Identification of small globular proteins found on bare mica. AFM images of
566 small particles observed on bare mica (A) before and (B) after alkaline treatment of
567 purified magnetosomes. (C) An AFM micrograph of the particles removed from the
568 purified magnetosomes with alkaline buffer. (D) An AFM image of particles observed
569 on bare mica around magnetosomes from *ΔmamA* mutant. (E) Histogram for the heights
570 of small particles observed around the magnetosomes. The black curve represents the fit
571 to the sum of two Gaussians (shown individually in white lines; 3.0 ± 0.6 nm and $6.6 \pm$
572 0.8 nm). (F) Histogram for the heights of the particles removed from magnetosomes by
573 alkaline treatment. The curve represents the fit to a Gaussian distribution (2.6 ± 0.6 nm).
574 (G) Histogram for the heights of particles observed around magnetosomes from *ΔmamA*
575 mutant. (H) Silver-stained SDS-PAGE gel of magnetosomal protein absorbed on bare
576 mica (lane 1), and proteins extracted from the purified magnetosomes (lane 2).
577 Precision Plus protein standard was used (Lane M). (I) Immunoblot analysis with

578 anti-MamA antibody. The proteins extracted from bare mica and magnetosomes were
579 loaded on lanes 1 and 2, respectively. Magnetosomes were prepared from wild type *M.*
580 *magneticum* AMB-1 except for panel D and G.

581

582 Fig. 3. Dissection of magnetosomes adsorbed on bare mica. The surface was scanned at
583 1.0 s/frame with the number of pixels of 256×256. This nanodissection treatment
584 exposed the underlying sheet-like structure (asterisks). Also, small particles (which
585 were measured ~3 nm in height) appeared on the mica surface (arrowheads). The
586 numbers indicate frame number.

587

588 Fig. 4. Oligomerization of MamA. (A) SDS-PAGE analysis of binding magnetosomal
589 proteins on the His-MamA affinity column. The protein bands were visualized by silver
590 staining. Lane 1: solubilized magnetosome-associated proteins. Lane 2: the eluted
591 proteins from BSA column. Lane 3: the eluted proteins from His-MamA affinity
592 column. The 24-kDa protein (arrow) was identified as MamA_{MS-1} by immunoblotting.
593 The arrowhead shows that the His-MamA came off from the column. (B) Pull down
594 assays. MamA_{MS-1} (arrow) was co-precipitated from solubilized
595 magnetosome-associated proteins with His-MamA (arrowhead) binding to Ni-NTA
596 resin. The gel was stained with Coomassie Brilliant Blue G-250. (C) AFM image of
597 His-MamA oligomer on AP-mica. (D) High magnification image of His-MamA
598 oligomer on AP-mica. AFM images were recorded at an imaging rate of 1 s/frame and
599 the number of pixels was 256 × 256.

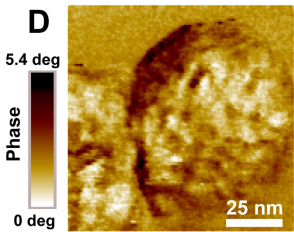
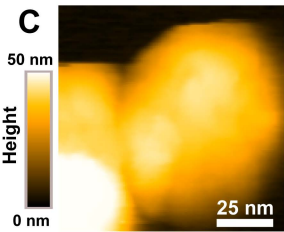
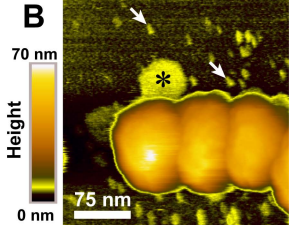
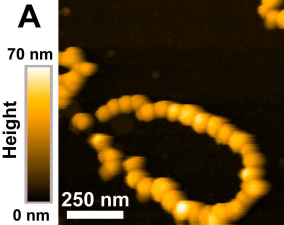
600

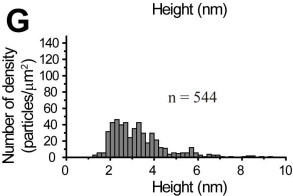
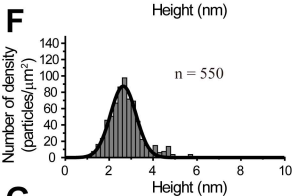
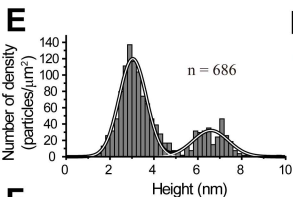
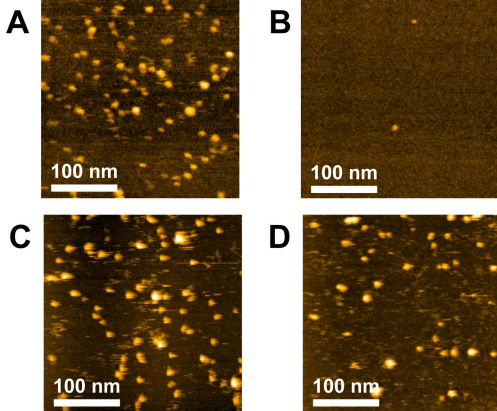
601 Fig. 5. AFM images of immuno-labeled magnetosomes. Magnetosomes labeled with

602 (A) anti-MamA antibodies and (B) pre-immuno serum. (C and D) Surface profile along
603 the lines indicated in (A) and (B). Magnetosomes labeled with anti-MamA antibodies
604 after (E) the alkaline treatment and (F) the His-MamA reconstruction. AFM images
605 were recorded at an imaging rate of 3 s/frame and the number of pixels of (A and B)
606 200×200 and (E and F) 256×256.

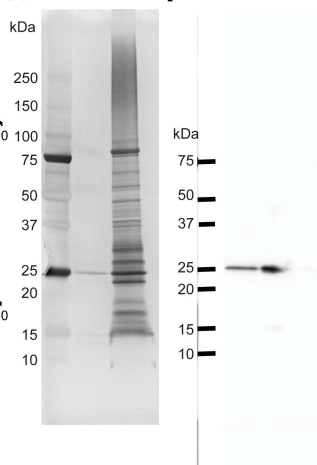
607

608 Fig. 6. Histogram of the center-to-center distance between adjacent magnetosomes. (A)
609 From wild type: intact; magenta, alkaline treated; green, MamA reconstructed; cyan. (B)
610 From *ΔmamA* mutant: intact; magenta, the alkaline treated; green. The curves indicate
611 fit to the Gaussian distributions.





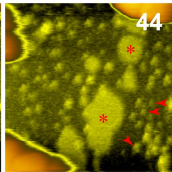
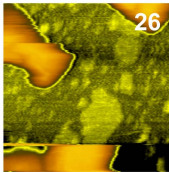
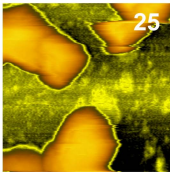
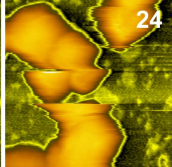
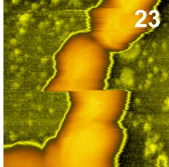
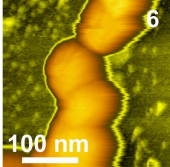
H M 1 2 **I** M 1 2

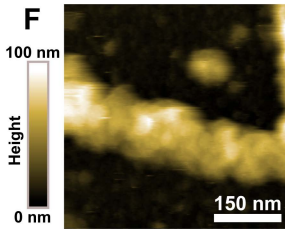
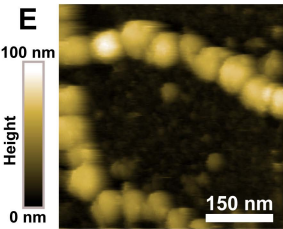
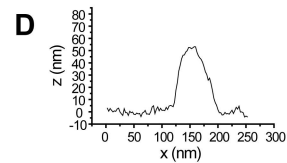
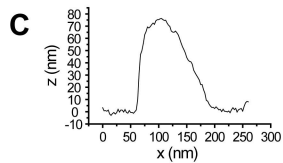
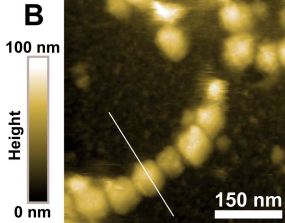
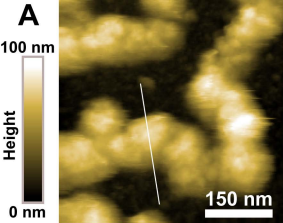


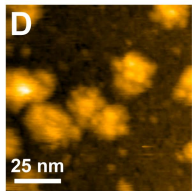
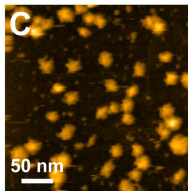
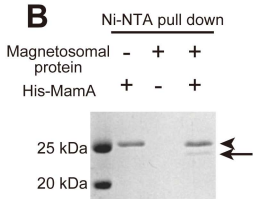
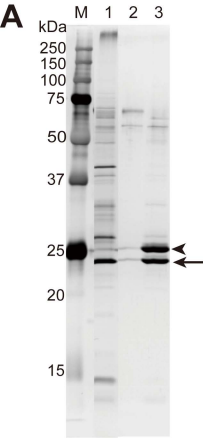
70 nm



0 nm







0 nm Height 8.4 nm

0 nm Height 8.8 nm

